Journal of Fluids and Structures 53 (2015) 2–14

Contents lists available at ScienceDirect

Journal of Fluids and Structures

journal homepage: www.elsevier.com/locate/jfs

A review of rotating cylinder wake transitions

A. Rao [a,*], A. Radi [a], J.S. Leontini [b], M.C. Thompson [a], J. Sheridan [a], K. Hourigan [a,c]

[a] Fluids Laboratory for Aeronautical and Industrial Research (FLAIR), Department of Mechanical and Aerospace Engineering, Monash University, Clayton 3800, Australia
[b] Department of Mechanical Engineering and Product Design Engineering, Swinburne University of Technology, John St, Hawthorn 3162, Australia
[c] Division of Biological Engineering, Monash University, Clayton 3800, Australia

ARTICLE INFO

Article history:
Received 11 November 2013
Accepted 17 March 2014
Available online 4 June 2014

Keywords:
Wakes
Flow stability
Vortex street
Transition

ABSTRACT

Recent work on the flow past a rotating cylinder is reviewed and further investigated at low Reynolds numbers. The various two- and three-dimensional transitions that occur as the rotation rate is increased are detailed. Two steady states, steady state I and steady state II, are identified based on the physical characteristics of the wake and the drag force on the body. Steady state I occurs at lower rotation rates, while state steady state II occurs at higher rotation rates. Linear stability analysis shows that two three-dimensional modes become unstable on steady state I and steady state II. Floquet stability analysis of the unsteady base flows that occur at very low rotation rates shows the presence of five three-dimensional modes. The curves of marginal stability are presented, followed by a comparison of numerical simulations to their experimentally obtained counterparts. Furthermore, the spatio-temporal characteristics of each mode and the likely underlying physical mechanisms are briefly discussed.

1. Introduction

In this study, we review the recent developments in the understanding of the wake of an isolated rotating cylinder in freestream at low Reynolds numbers. The flow is a function of two parameters: the flow Reynolds number (Re) and non-dimensionalised rotation rate (α). The Reynolds number is given by $\mathrm{Re} = UD/\nu$, where U is the incoming freestream velocity, D is the cylinder diameter and ν is the kinematic viscosity of the fluid. The rotation rate is defined by $\alpha = \omega D/2U$, where ω is the angular velocity of the cylinder. The rotation rate is also equivalent to twice the ratio of the surface speed of the cylinder to the freestream velocity. In this paper, we examine the various flow transitions that occur for $\alpha < 7$ and $\mathrm{Re} \leq 400$.

The wakes from a non-rotating circular cylinder in the low Reynolds number range, together with the various transitions that occur, have been extensively documented. Amongst others, a comprehensive review detailing the steady and unsteady regimes has been presented by Williamson (1996a). Unsteady flow is observed on increasing the Reynolds number past $\mathrm{Re} \simeq 47$, which is characterised by the shedding of vortices alternately from the top and bottom separating shear layers to form a vortex street. This is commonly referred to as Bénard–von Kármán shedding. On further increasing the Reynolds number, secondary three-dimensional vortices begin to form on the otherwise two-dimensional wake at $\mathrm{Re} \simeq 190$. The wake vortices develop spanwise waviness of approximately four cylinder diameters, and this state is referred to as *mode A*

* Corresponding author.
E-mail address: anirudh.rao@monash.edu (A. Rao).

http://dx.doi.org/10.1016/j.jfluidstructs.2014.03.010
0889-9746/

shedding (Williamson, 1988). Another three-dimensional mode, mode B, appears with a spanwise wavelength of $0.8D$ on further increasing the Reynolds number above Re=230–240 (Williamson, 1988; Wu et al., 1996a, 1996b, 1994). Numerical investigations by several research groups (e.g., Barkley and Henderson, 1996; Thompson et al., 1996; Zhang et al., 1995) observed the associated three-dimensional structures. Mode A is observed to grow primarily in the vortex cores, while mode B grows in the braid shear layers connecting the opposite-signed vortex cores. These two modes do not introduce any secondary frequencies in the wake, although in their saturated state they do modify the primary wake frequency slightly. The analogues of modes A and B have also been detected in the wakes of other bluff bodies, such as square cylinders (Robichaux et al., 1999) and elongated bluff bodies (Ryan et al., 2005).

Other modes which do introduce new frequencies have also been observed in the wakes of bluff bodies. These modes are quasi-periodic in nature, and the secondary frequencies can be due to modulated standing waves or due to travelling waves in the spanwise direction. Because of their quasi-periodic nature, they have been referred to as QP modes (Blackburn and Lopez, 2003; Blackburn et al., 2005).

Another three-dimensional mode can be observed when the wake symmetry is altered, as in the wakes behind tori of different aspect ratios (Sheard et al., 2004a, 2004b, 2005), inclined square cylinders (Sheard et al., 2009; Sheard, 2011), and the asymmetric wakes found behind oscillating cylinders (Leontini et al., 2007). Typically, this mode has a spanwise wavelength between modes A and B and is $2T$ periodic (i.e., subharmonic), where T is the period of vortex shedding. It is referred to as *mode C*, and was also observed for a non-rotating cylinder when a trip wire was placed in the wake (Zhang et al., 1995; Yildirim et al., 2013a, 2013b) for $165 \leq \mathrm{Re} \leq 300$.

Cylinder rotation brings about asymmetrical wake flow, leading to a net lift force. This is commonly known as the Magnus effect (Prandtl, 1926). Flow past rotating cylinders at low Reynolds numbers has been investigated by several research groups (Mittal and Kumar, 2003; Stojković et al., 2002, 2003; Kang et al., 1999; Akoury et al., 2008; Pralits et al., 2010, 2013), who observed two distinct shedding regimes. At low rotation rates ($\alpha \lesssim 2$), the classical Bénard–von-Kármán (BvK) vortex street is observed (also known as *mode I shedding*), where vortices are shed alternatively. The second shedding regime (also known as *mode II shedding*) occurs at higher α over a narrow band. In this regime, single-sided vortex shedding occurs with a period much longer than for mode I shedding. Recent experimental investigations by Kumar et al. (2011) and Balcarová (2011) confirmed the existence of these two shedding regimes.

Very few investigations have been carried out on the development of three-dimensionality in rotating cylinder wakes. Three-dimensional DNS was performed by Akoury et al. (2008) at low rotation rates of $\alpha < 1.5$. They observed that the onset of the mode A instability was delayed to higher Reynolds numbers as the rotation rate was increased. At $\alpha=0.5$, the critical Reynolds number was predicted to be approximately 220, and at $\alpha=1.5$, Re=200, the flow remained two-dimensional. Mittal (2004) performed three-dimensional simulations at $\alpha=5$, Re=200 with different end conditions and observed small spanwise structures, which were possibly due to centrifugal instabilities. Stability analysis and three-dimensional simulations were performed by Meena et al. (2011) at higher rotation rates; these showed that the flow was unstable to perturbations for $3 \leq \alpha \leq 5$ at Re=200.

Recent numerical investigations by Rao et al. (2013a, 2013b) showed several three-dimensional modes becoming unstable to spanwise perturbations in the steady and unsteady regimes of flow for $\mathrm{Re} \leq 400$. Five three-dimensional modes were found to be unstable in the mode I shedding regime, while four three-dimensional modes were observed in the steady regimes of flow for $\alpha \gtrsim 2$. The saturated state of these modes has been observed experimentally by Radi et al. (2013). The experimentally observed modes were in excellent agreement with those observed in the numerical simulations.

In this study, we review and present results from the linear stability analysis and present some comparative experimental visualisations. The remainder of this paper is organised as follows. In Section 2, the numerical formulation and the experimental setup are described, followed by the results from the stability analysis and a direct comparison to the experimental visualisations in Section 3. The conclusions summarise and provide a perspective on the findings.

2. Methodology

2.1. Numerical formulation

A spectral-element formulation was used to discretise the incompressible Navier–Stokes equations in two dimensions. The computational domain consists of quadrilateral macro-elements, which are further subdivided using internal node points distributed according to the Gauss–Legendre–Lobatto quadrature points. The velocity and pressure fields are represented by tensor products of Lagrangian polynomial interpolants. For smooth problems, as the polynomial order is increased, spectral convergence is achieved (Karniadakis and Sherwin, 2005). An unsteady solver employing a fractional time-stepping method was used to integrate the convection, pressure and diffusion terms of the Navier–Stokes equations. More details of this solver can be found in Thompson et al. (2006).

To investigate the three-dimensional stability of the flow to spanwise perturbations, linear stability analysis was employed. The linear stability equations were marched forward in time for initially random perturbations for a given wavelength. After some time, only the first few dominant amplifying or decaying modes remain. This method was used to obtain the fastest growing modes, and has previously been used to determine the onset of three-dimensionality for a variety of different problems, including oscillating cylinders (Leontini et al., 2007; Lo Jacono et al., 2010; Leontini et al., 2013) and rotating cylinders near a wall (Stewart et al., 2006, 2010; Rao et al., 2011). For a periodic base flow, the amplification factor of

a mode over a period is known as the Floquet multiplier (μ), and it provides a measure of the growth of the perturbation. If $|\mu| > 1$, the instability mode grows, and for $|\mu| < 1$ it decays. Neutral/marginal stability occurs for $|\mu| = 1$. The same process can be applied for steady base flows, which have an essentially arbitrary period.

The computational domain used in this study consisted of the cylinder in the centre, with the inlet, outlet and lateral boundaries being $100D$ from the cylinder to reduce blockage effects. Spatial resolution studies carried out on these domains at Re$=400$ indicated that the solutions converged for a spatial resolution of $N^2 = 8^2$, where N is the number of internal node points on each side of a macroelement. The force histories and shedding frequencies computed in the steady and unsteady regimes of flow were in good agreement with previous literature. These resolution studies are detailed in Rao et al. (2013a, 2013b).

2.2. Experimental setup

The experimental setup consisted of a stiff carbon-fibre cylinder of 5.8 mm diameter driven by a stepper motor in the FLAIR open surface water channel. The wetted length of the cylinder in the channel was approximately 130 times the cylinder diameter. The cylinder wobbling was kept within 2.5% of the cylinder diameter even for high rotation rates of $\alpha = 5$. This is within acceptable limits to not unduly influence the flow behaviour (Mittal, 2001). A platinum wire (50 μm) positioned five cylinder diameters upstream and parallel to the main cylinder axis was used for the generation of a sheet of hydrogen bubbles. The sheet passed the rotating cylinder and was entrained by the near wake, making the three-dimensional structures visible. A continuous laser sheet was used for illumination. The images were recorded with a digital camera and numerically processed to extract information on wavelengths and mode symmetries. More details on the experimental setup are described in Radi et al. (2013).

3. Results

3.1. Parameter space

The parameter space investigated in this study covers the ranges $0 \leq \alpha \leq 7$ and $0 \leq \mathrm{Re} \leq 400$. Fig. 1(a) shows the marginal stability curves for the many transitions on the Re, α plane. On this parameter map (i) transitions between steady states, (ii) transitions from a steady state to an unsteady state, and (iii) transitions from two-dimensional flow to three-dimensional flow, are marked. At each rotation rate, the critical values were obtained by interpolation between values of $|\mu|$ at α, Re points in the vicinity of the transition.

Fig. 1(a) can be roughly divided into three areas, depending on rotation rate. At lower rotation rates ($\alpha \lesssim 1.3$), the transition scenario is similar to that observed for a non-rotating cylinder, where with increasing Re, the flow undergoes transition to an unsteady state (BvK vortex shedding) from a steady state, followed by the transition to three-dimensionality via mode A, followed by a second possible three-dimensional transition to mode B at higher Reynolds numbers (Williamson, 1996b; Barkley and Henderson, 1996; Thompson et al., 1996).

For moderate rotation rates $1.5 \lesssim \alpha \lesssim 2$, multiple three-dimensional modes (modes C, D and G) that are not present in the stationary cylinder case bifurcate from the two-dimensional vortex shedding flow.

For high rotation rates $\alpha \gtrsim 2$, the BvK vortex shedding is suppressed, and is replaced by steady state I. A second single-sided vortex shedding mode, named mode II shedding, occurs over a small range of α, bifurcating from steady state I. (Rao et al., 2013a; Kang et al., 1999; Pralits et al., 2013; Stojković et al., 2002, 2003). The exact range is a function of Re. However, this two-dimensional single-sided shedding is predicted in a region of the parameter space where steady state I has already been through a bifurcation to a three-dimensional state, and so it is unclear as to how this single-sided shedding will physically manifest. Two three-dimensional modes grow on steady state I, being modes E and F.

At even higher rotation rates $\alpha > 5$, steady state I is replaced by steady state II. Two three-dimensional modes, mode E′ and mode F′, are found to grow on this steady state. In Fig. 1(a), the existence region for mode E′ is bounded by a dashed line to indicate that its computed growth rate is very sensitive to computational domain size.

The regions where these modes are unstable are marked by unique colours on the parameter space plots in Fig. 1(c)–(i). These smaller images were used to obtain the composite diagram, Fig. 1(a).

In the following sections, the steady two-dimensional base flows of interest are described. Then, details of the three-dimensional modes bifurcating from these steady flows and the BvK vortex shedding are provided. These details are supplemented by the three-dimensional reconstruction of the modes and their saturated experimental counterparts obtained from flow visualisation experiments.

3.2. Steady state I and II

Two distinct steady states are observed in the wake of a rotating cylinder as described by Mittal and Kumar (2003) and Pralits et al. (2010). These two steady states can be distinguished by the structure of the wake, streamwise location of the stagnation point and the mean drag coefficient. The boundary of demarcation of the two steady states extends to higher rotation rates at lower Reynolds numbers. As detailed in Rao et al. (2013b), the shear layers in steady state I form a “tail-like” structure, while the steady state II wake is distinguished by shear layers wrapped around the rotating cylinder.

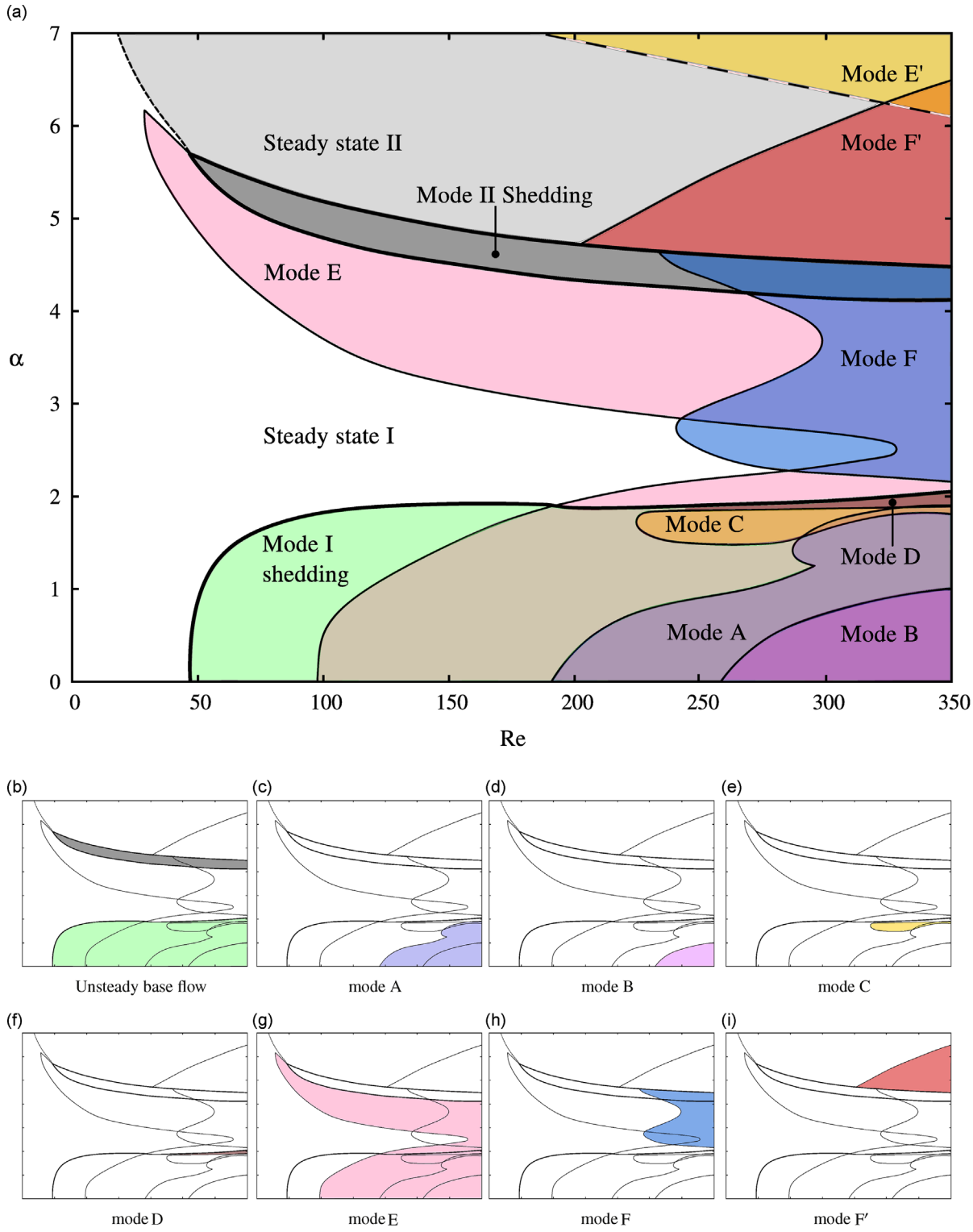

Fig. 1. (a) Marginal stability diagram of the Re, α parameter space, showing the various bifurcations for $\alpha \leq 7$, $\mathrm{Re} \leq 350$. Regions of unsteady flow, and the regions of instability of three-dimensional modes A–F′ are assigned a unique colour as shown in subfigures (b)–(i), which make up the composite image (a). Mode E′ is shown by dashed lines to indicate that the boundary of this mode is very sensitive to the computational domain size. Mode G occurs at discrete locations and is not shown here. (For interpretation of the references to colour in this figure caption, the reader is referred to the web version of this paper.)

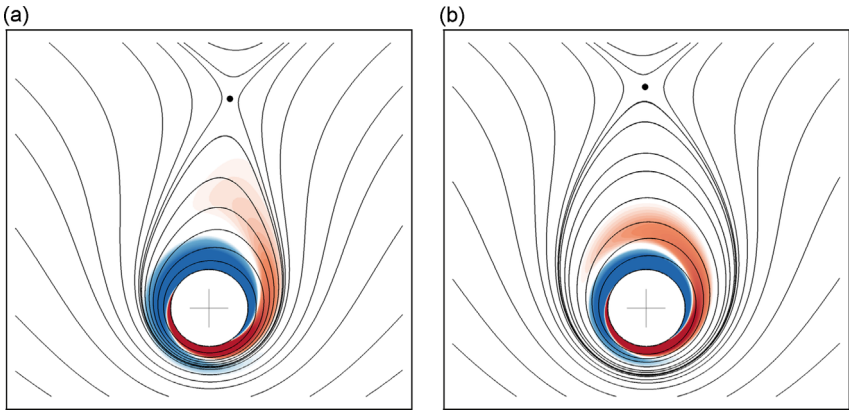

Fig. 2. Visualisation of the two steady states at $\alpha=6.25$. Base flow vorticity contours between levels $\pm 4D/U$ are overlaid with streamlines for steady state I at Re$=25$ (a) and steady state II at Re$=40$ (b). The stagnation point (x_s/D) is denoted by filled circles (●) while cross-hairs mark the centre of the cylinder. Flow is from left to right, with the cylinder rotating anticlockwise.

The stagnation point, which lies above the cylinder, moves upstream as the flow undergoes transition from steady state I to steady state II. This is accompanied by a change in mean drag coefficient.

Shown in Fig. 2 are the base flow vorticity contours at $\alpha=6.25$. In steady state I, the shear layers form a tail-like structure, with the stagnation point (x_s/D) downstream of the cylinder at Re$=25$, while steady state II shows the shear layers wrapped around the cylinder and the location of the stagnation point upstream of the centre of the cylinder.

3.3. Mode A instability

For a non-rotating cylinder, the mode A instability was first characterised through the experimental investigations of Williamson (1988), and was subsequently predicted by the linear stability analysis of Barkley and Henderson (1996). For $0 \leq \alpha \lesssim 1.25$, mode A is the first three-dimensional mode to become unstable to spanwise perturbations; however, the onset of the mode A instability is delayed to higher Reynolds numbers as the rotation rate is increased. At higher rotation rates, mode A co-exists with other three-dimensional modes. The Floquet multiplier is real and positive, and the spanwise wavelength for this instability is $\lambda \simeq 4D$. The physical mechanism of this instability has previously been attributed to an elliptic instability of the forming vortex cores (Leweke and Williamson, 1998; Thompson et al., 2001).

Shown in Fig. 3(a) and (c) are the spanwise perturbation vorticity contours at values close to the maximum growth rate and the three-dimensional reconstruction of this mode from the linear stability analysis, respectively. An experimental visualisation is shown in Fig. 3(e) for a non-rotating cylinder at Re$=175$. For $\alpha \leq 1$, mode A was very difficult to visualise in the experiments, although it may have contributed to the early transition of mode B.

3.4. Mode B instability

At the same rotation rate, the mode B instability becomes unstable at Reynolds numbers higher than that for the mode A instability. Similar to mode A, the onset of mode B is delayed to higher Reynolds numbers as the rotation rate is increased from $\alpha=0$ to $\alpha=1$. The characteristic wavelength of this instability is $\lambda \simeq 0.8D$ and its Floquet multiplier is real and positive.

Shown in Fig. 3(b) and (d) are the spanwise perturbation contours and a three-dimensional reconstruction, respectively. Significant perturbation amplitude is apparent in the strained braid regions between the vortex cores. Fig. 3(f) shows an experimental visualisation of the mode B instability at Re$=275$.

3.5. Mode C instability

As the rotation rate is increased to $\alpha \gtrsim 1.3$, the wake becomes clearly asymmetric. Wake asymmetry has previously been known to give rise to a subharmonic mode, termed mode C (Blackburn and Sheard, 2010). This mode has previously been observed in the wake of a torus (Sheard et al., 2003, 2004a, 2005), inclined square cylinders (Sheard et al., 2009; Sheard, 2011) and in the wake of non-rotating circular cylinders using a trip wire (Zhang et al., 1995; Yildirim et al., 2013b).

Mode C becomes unstable for $1.5 \leq \alpha \leq 1.85$ for Re ≥ 240 and exists in a nearly closed region of the parameter space. The Floquet multiplier is purely real and negative, indicating its precise subharmonic nature.

Visualisations of the spanwise perturbation vorticity taken one period apart for $\alpha=1.7$, Re$=275$ show that the contours alternate in sign, as shown in Fig. 4(a) and (b). Fig. 4(d)(i) and (ii) shows the experimental visualisation at the same point in the parameter space, while Fig. 4(c)(i) and (ii) shows the three-dimensional reconstruction of the mode one period apart. These diagrams indicate that the vortices are shifted by half a wavelength along the spanwise direction over each base flow period, thereby showing the $2T$ periodicity of this mode.

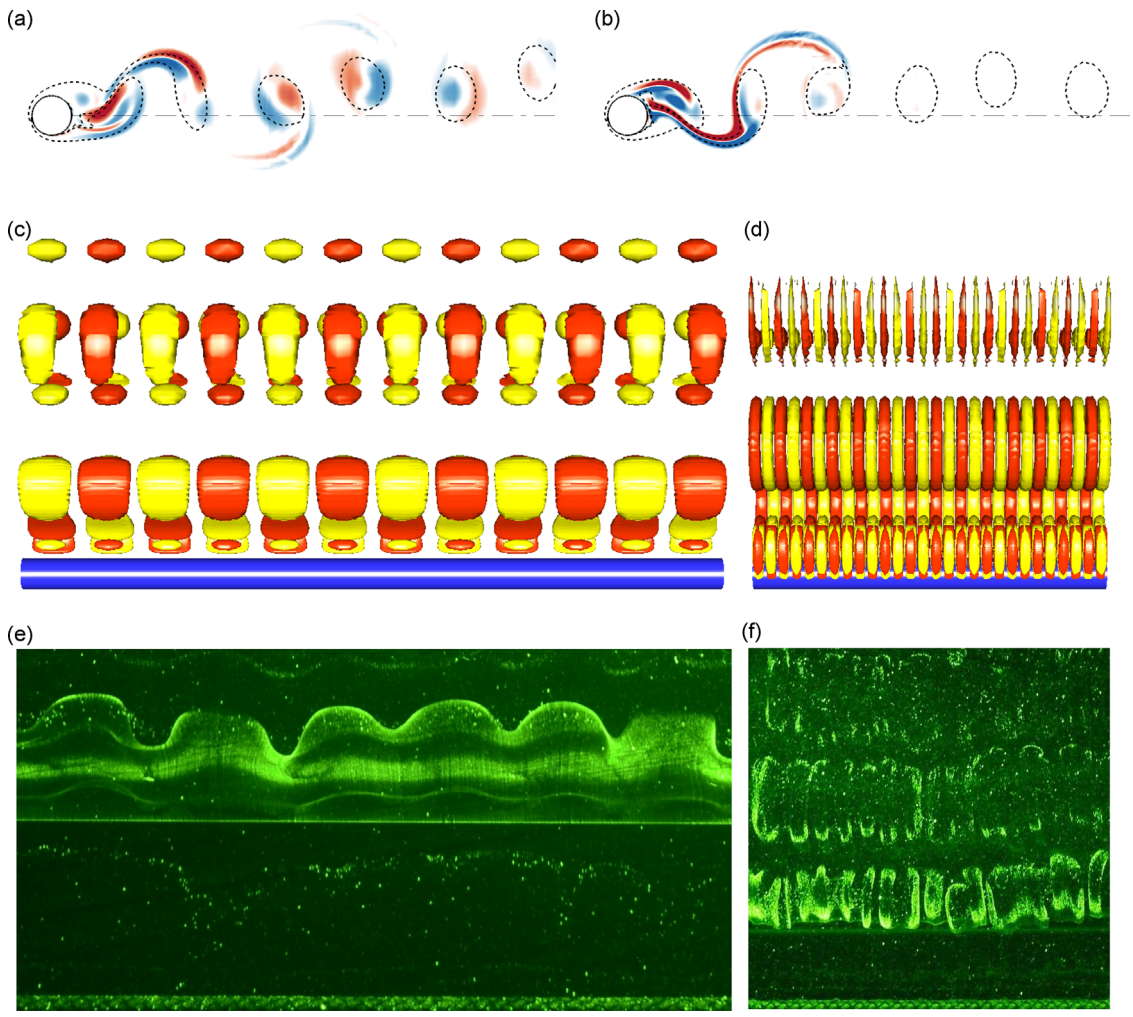

Fig. 3. (a), (b) Visualisation of the spanwise perturbation vorticity contours for the mode A and mode B instability at the rotation rates and Reynolds numbers specified. Perturbation vorticity contour levels in (a) and (b) are between $\pm 0.1D/U$ (although arbitrary), with base flow vorticity contours between levels $\pm 1D/U$ overlaid. Flow is from left to right in these images, with the cylinder rotating anticlockwise. A dashed line downstream and through the centre of the cylinder is drawn to show the wake asymmetry. Images (c) and (d) show the three-dimensional reconstruction of the above cases for modes A and B, respectively, in plan view. Hydrogen bubble flow visualisations for the non-rotating cylinder are provided in the next two images. The first (e) shows mode A at Re=175 with $\lambda_{exp}/D \simeq 3.5$, while (f) shows mode B at Re=275 and $\lambda_{exp}/D \simeq 0.96$ (f). Images (c), (e) and (d), (f) are on the same scale, with flow from the bottom to the top. The platinum wire is positioned downstream of the cylinder in (e) and (f). Experimental images are reproduced from Radi et al. (2013). (a) α=0.75, Re=240, λ/D=3.75 and (b) α=0.75, Re=320, λ/D=0.8.

3.6. Mode D and E instabilities

The mode D instability occurs on an unsteady base flow in a small region of the parameter space for $\alpha \gtrsim 1.9$. This mode is associated with high frequency shedding of vortices, which are formed in the strained shear layers. This mode has a positive real Floquet multiplier, with its spatio-temporal characteristics similar to the mode A instability. However, the spanwise wavelength is $\lambda \simeq 2D$.

Fig. 5(a) and (c) shows the spanwise perturbation vorticity contours at values close to the maximum growth rate and the corresponding three-dimensional reconstruction, respectively, while Fig. 5(e) shows the experimental flow visualisation of the mode D instability with a laser sheet illuminating the shed vortices.

The mode E instability occurs on the steady base flow at rotation rates of $\alpha \gtrsim 2$. This three-dimensional mode has a purely real and positive growth rate, with a spanwise wavelength of $\lambda \simeq 2D$. In terms of mode shape, it appears very similar to mode D, except that it occurs on a steady base flow, and hence it is presumably an extension of mode D into the steady base flow regime. The variation of the critical Reynolds number at higher rotation rates has previously been shown in Rao et al. (2013b) and Pralits et al. (2013).

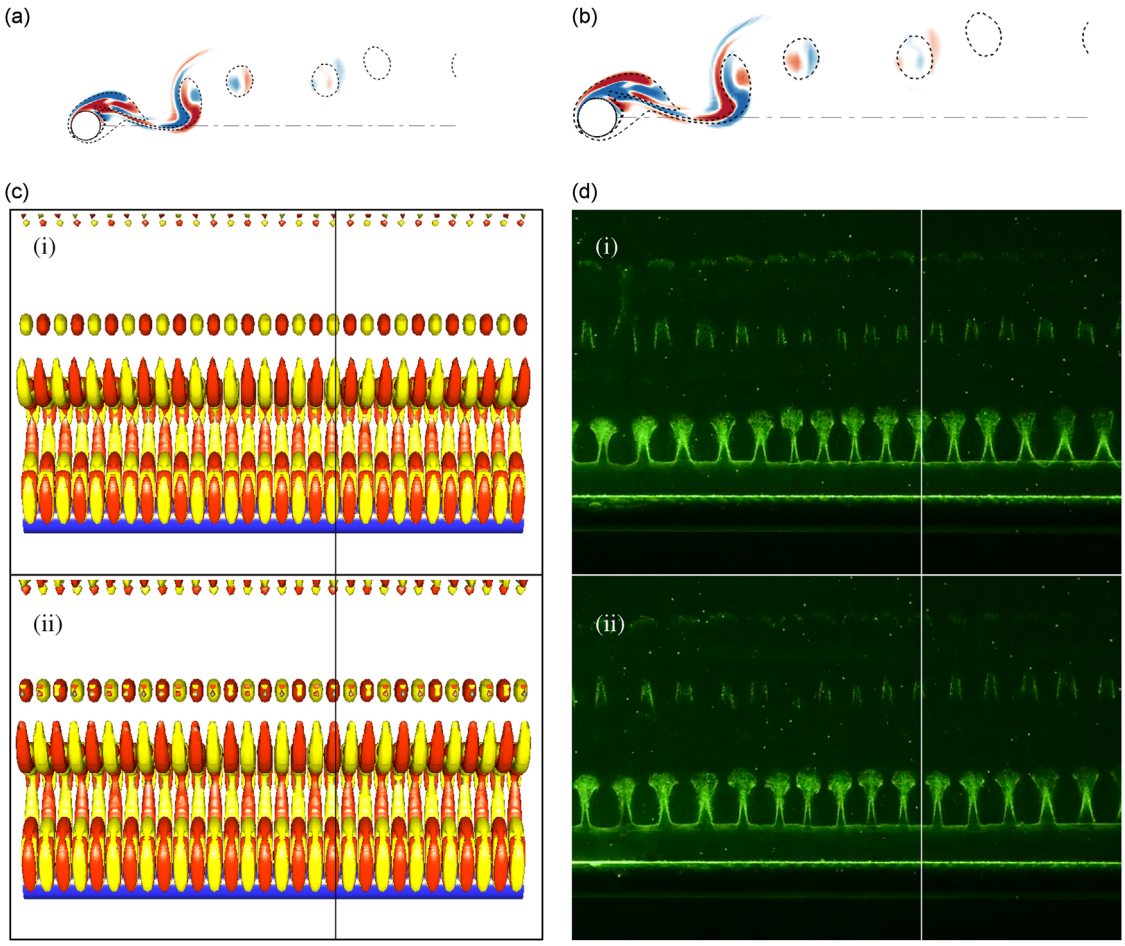

Fig. 4. (a), (b) Visualisation of the spanwise perturbation vorticity contours for the mode C instability at $\alpha = 1.7$, Re$=275$, $\lambda/D = 1$, showing the subharmonic character. Contour shading as per Fig. 3. Flow is from left to right in (a) and (b), with the cylinder rotating anticlockwise; while (c) shows the three-dimensional reconstruction of (a) and (b) over two consecutive periods. The experimental visualisation of the mode C instability at $\alpha = 1.7$, Re$=275$, over $z/D = 15$ is shown in (d). The black line in (c) and the white line in (d) can be used as a guide to follow the same spatial location in (i) and (ii), respectively. In both these cases, the secondary vortices are shifted by half a wavelength in the spanwise direction. The flow is from bottom to top in (c) and (d). (a) $t = t_0$, (b) $t = t_0 + T$.

Fig. 5(b) and (d) shows the perturbation vorticity contours at values close to the maximum growth rate and the three-dimensional reconstruction of the mode E instability, respectively. Fig. 5(f) shows the experimental visualisation of the instability with the laser sheet illuminating the elongated shear layers.

The instability mechanisms of mode D and mode E are believed to be due to a hyperbolic instability in the strained shear layers in the near wake of the cylinder, as has been examined and discussed in Rao et al. (2013a, 2013b). At higher rotation rates ($\alpha \gtrsim 5.3$), the onset of the mode E instability occurs at increasingly lower Reynolds numbers ($\mathrm{Re}_c \lesssim 50$). However, mode E remains unstable over a narrow range of Reynolds numbers at these high rotation rates, and stabilises prior to the transition to steady state II.

At lower rotation rates ($\alpha \lesssim 1.9$), where the base flow is naturally unsteady due to BvK vortex shedding, an artificially stabilised steady two-dimensional base flow was obtained using a steady spectral-element solver. The resulting flow is steady state I. The existence of mode E was tested on this base flow. Shown in Fig. 6 are the spanwise perturbation contours of mode E in this stabilised range. These previously unpublished results, along with the data shown in Fig. 7, indicate that the critical Reynolds number for the onset of mode E over this stabilised range ($\alpha \lesssim 1.9$) monotonically decreases from $\mathrm{Re}_c \simeq 190$ at $\alpha \simeq 1.9$ to $\mathrm{Re}_c \simeq 100$ at $\alpha = 0$. The critical spanwise wavelength increases with decreasing α in this range.

Combining these previously unpublished results with the results from Rao et al. (2013b), the overall variation of the critical spanwise wavelength and Reynolds number for the mode E instability is shown in Fig. 7(a). The critical Reynolds number increases on increasing the rotation rate from $\mathrm{Re}_c \simeq 95$ at $\alpha = 0$ to $\mathrm{Re}_c \simeq 330$ at $\alpha = 2.5$, before decreasing to lower values with further increases in rotation rate ($\mathrm{Re}_c \simeq 30$ at $\alpha = 6.15$). However, the critical spanwise wavelength decreases on increasing the rotation rate from $\lambda/D \simeq 6$ at $\alpha = 0$ to $\lambda_c/D \simeq 1.4$ at $\alpha \simeq 2.5$, before increasing to very high values with further increases in rotation rate ($\lambda/D \simeq 12$ at $\alpha = 6.15$). The three-dimensional reconstruction of the mode E instability (Fig. 7(b)–(h))

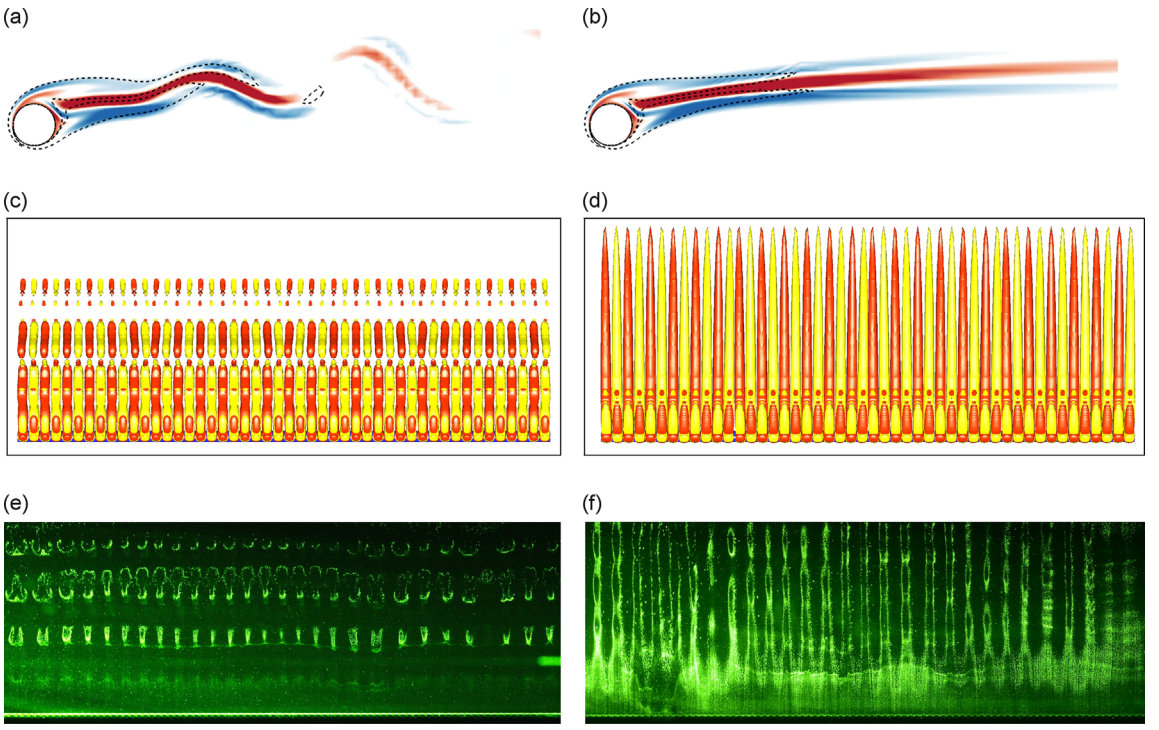

Fig. 5. (a), (b) Visualisation of the spanwise perturbation vorticity contours for the mode D and mode E instabilities at the specified parameters. Contour shading as per Fig. 3. Flow is from left to right in (a) and (b) with the cylinder rotating anticlockwise. Images (c) and (d) show the three-dimensional reconstruction of the modes in (a) and (b) in plan view, respectively. Experimental visualisations of the modes D and E at the specified parameters are shown in (e) and (f). Flow is from the bottom to the top in images (c), (d), (e) and (f), and these images are visualised for a spanwise distance of $z/D = 48$. Experimental images are reproduced from Radi et al. (2013). (a) $\alpha = 1.9$, $Re = 280$, $\lambda/D = 2$, (b) $\alpha = 2$, $Re = 280$, $\lambda/D = 2$, (e) $\alpha = 1.9$, $Re = 250$, $\lambda_{exp}/D \simeq 2$ and (f) $\alpha = 2.1$, $Re = 250$, $\lambda_{exp}/D \simeq 1.8$.

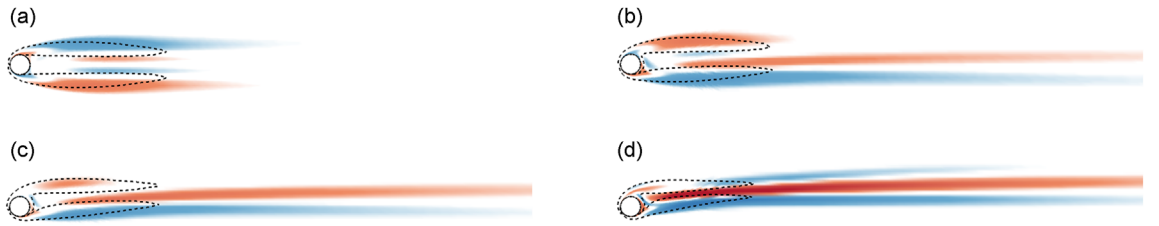

Fig. 6. Spanwise perturbation vorticity contours of the mode E instability at the specified values of rotation rates and Reynolds numbers. Contour shading as per Fig. 3. Flow is from left to right and the cylinder is rotating anticlockwise. (a) $\alpha = 0$, $\mathrm{Re} = 100$, $\lambda/D = 6$. (b) $\alpha = 0.5$, $\mathrm{Re} = 100$, $\lambda/D = 5.5$. (c) $\alpha = 1$, $\mathrm{Re} = 120$, $\lambda/D = 5$. (d) $\alpha = 1.5$, $\mathrm{Re} = 160$, $\lambda/D = 3$.

over a spanwise distance of $18D$ shows this variation. The maximum value of the critical Reynolds number and the minimum value of the critical spanwise wavelength both occur at the value of the rotation rate at which there is a distinct change in base flow. This distinct change is the disappearance of the upper recirculation region in the wake as the rotation rate is increased beyond this value (Rao et al., 2013b).

Closer examination of Fig. 6(a) reveals that the perturbation contours show high amplitude in the shear layers in the recirculation zone behind the cylinder. These contours resemble those observed for a non-rotating circular cylinder translating along a solid wall (Rao et al., 2011; Stewart et al., 2006, 2010; Hourigan et al., 2013; Rao et al., 2013c, 2013d). In those cases, the flow becomes three-dimensional prior to the onset of the unsteady flow. Furthermore, the spatio-temporal characteristics of that mode and mode E are similar.

3.7. *Mode F instability*

The mode F instability develops on steady state I for rotation rates $\alpha \geq 2.25$, and occurs at lower Reynolds numbers as the rotation rate is increased. The spanwise wavelength at onset is $\lambda \simeq 0.45D$, and the stability multiplier is complex, indicating

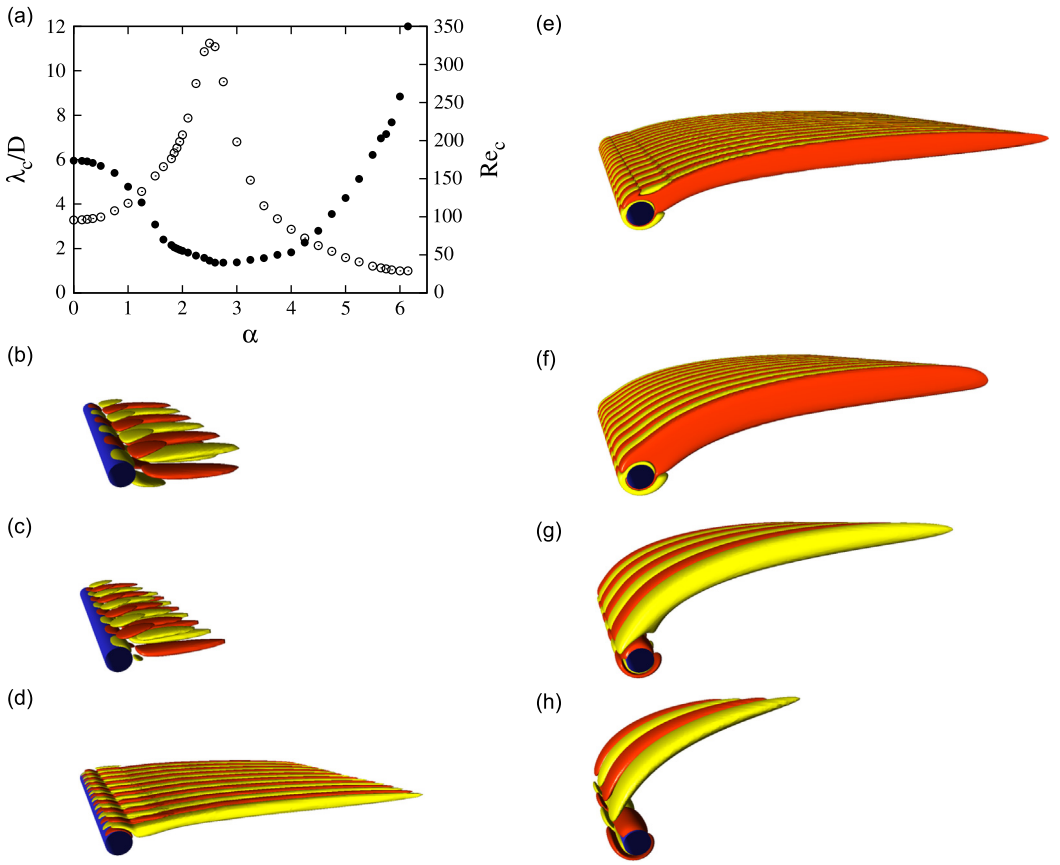

Fig. 7. (a) Variation of the critical spanwise wavelength (●) and critical Reynolds numbers (○) of the mode E instability with rotation rate. Figs. (b)–(h) show the three-dimensional reconstruction of the mode E instability over a spanwise distance of $z/D=18$ at the specified parameter values: (b) $\alpha=0$, Re=100, $\lambda/D=6$, (c) $\alpha=1$, Re=120, $\lambda/D=4.5$, (d) $\alpha=2$, Re=220, $\lambda/D=2$, (e) $\alpha=3$, Re=220, $\lambda/D=1.2$, (f) $\alpha=4$, Re=100, $\lambda/D=1.8$, (g) $\alpha=5$, Re=65, $\lambda/D=4.5$ and (h) $\alpha=6$, Re=33, $\lambda/D=9$. Flow is from left to right in these plots and the cylinder is rotating anticlockwise.

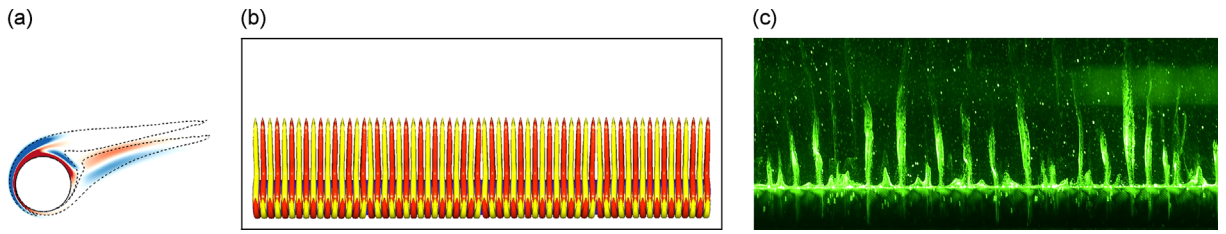

Fig. 8. (a) Visualisation of the spanwise perturbation vorticity contours for the mode F instability at $\alpha=2.25$, Re=320, $\lambda/D=0.4$. Contour shading as per Fig. 3. Flow is from left to right in (a) with the cylinder rotating anticlockwise. The three-dimensional reconstruction of the mode in plan view is shown in (b). An experimental visualisation of the mode D instability at $\alpha=2.3$, Re=275, $\lambda_{exp}/D\simeq 0.5$ is presented in (c). Flow is from bottom to top in (b) and (c), and these images are visualised for a spanwise distance of $z/D\simeq 12.8$. The experimental image is reproduced from Radi et al. (2013).

that the mode oscillates, as either a standing or travelling wave along the cylinder span. The physical mechanism of this three-dimensional mode has been attributed to a centrifugal instability (Rao et al., 2013a), with the perturbations growing in the boundary layer of the rotating cylinder.

Shown in Fig. 8(a) and (b) are the spanwise perturbation vorticity and its three-dimensional reconstruction, respectively. Fig. 8(c) shows the experimental flow visualisation at $\alpha=2.3$, where this mode is believed to co-exist with mode E.

3.8. *Mode F′ instability*

Mode F′ grows on steady state II base flow. With characteristics similar to the mode F instability, the three-dimensionality grows in the entrained shear layers on the surface of the rotating cylinder. The critical Reynolds number for the onset of mode F′ monotonically increases as the rotation rate is increased, with a corresponding decrease in the spanwise wavelength. The stability multiplier associated with this mode is complex, suggesting a spanwise movement

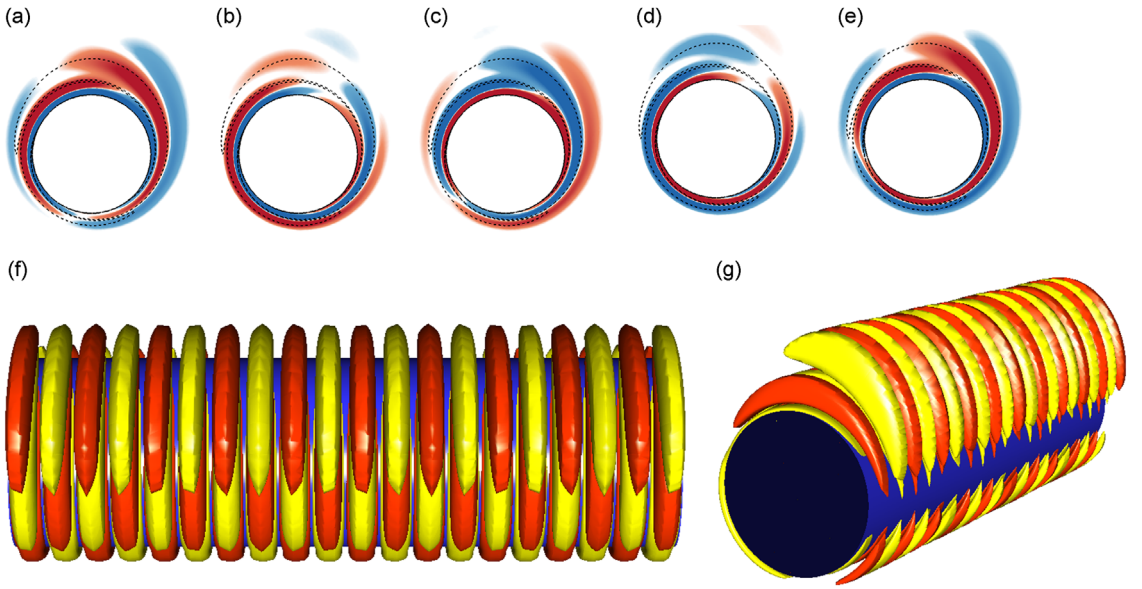

Fig. 9. (a)–(e) Visualisation of the spanwise perturbation vorticity contours for mode F′ at $\alpha=5.25$, Re$=240$, $\lambda/D=0.35$. Contour shading as per Fig. 3. Flow is from left to right in these images, with the cylinder rotating anticlockwise. Here (f) and (g) show the spanwise projection of mode F′ in top and perspective views, respectively, for a spanwise distance of $3.5D$, corresponding to ten wavelengths of the instability. Flow is from bottom to top in (f) and from left to right in (g). (a) $t=t_0$, (b) $t=t_0+0.5T$, (c) $t=t_0+T$, (d) $t=t_0+1.5T$, (e) $t=t_0+2T$, (f) top view and (g) perspective view.

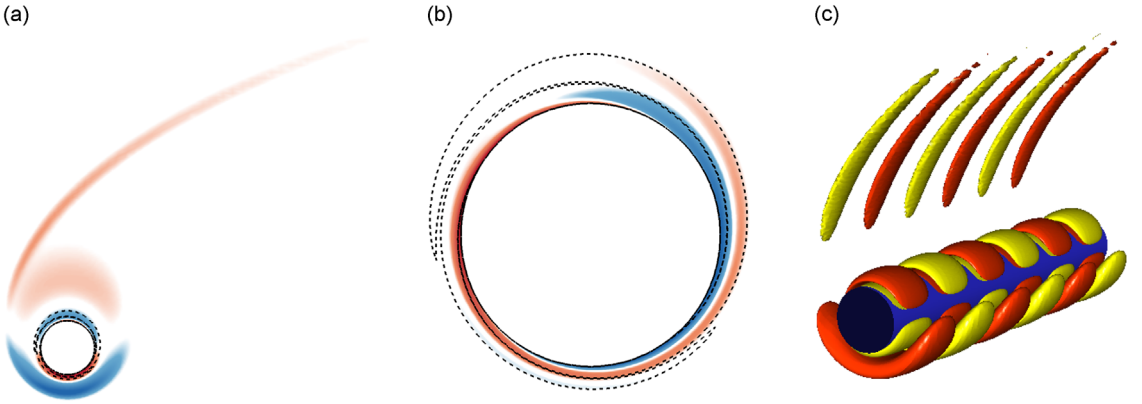

Fig. 10. (a) Streamwise and (b) spanwise perturbation vorticity contours at $\alpha=6.15$, Re$=340$, $\lambda/D=2.4$, respectively. Contour shading as per Fig. 3. (c) Three-dimensional reconstruction of the mode E′ instability for the above case visualised over a spanwise distance of $7.2D$, corresponding to three wavelengths of the instability. Flow is from left to right and the cylinder is rotating anticlockwise.

similar to mode F. These aspects have been quantified in Rao et al. (2013b). Shown in Fig. 9 are the spanwise perturbation vorticity contours at $\alpha=5.25$, Re$=240$. The spanwise movement of this mode means it repeats approximately, but not exactly, every two base flow periods.

3.9. *Mode* E′ *instability*

Mode E′ was observed at high rotation rates of $\alpha \gtrsim 6.15$ on steady state II base flow. It shares similar characteristics with mode E instability of steady state I, including spatial distribution and general shape of the perturbation field, and spatio-temporal symmetries. The critical Reynolds number for the onset of this mode decreases as the rotation rate is increased while the critical spanwise wavelength at onset increases. For a given rotation rate, the values of the stability multiplier are very close to unity over a large range of Reynolds numbers. Fig. 10(a) and (b) shows the streamwise and spanwise perturbation contours at $\alpha=6.15$, Re$=340$, $\lambda/D=2.4$, respectively. The three-dimensional reconstruction of this mode is shown in Fig. 10(c) in perspective view.

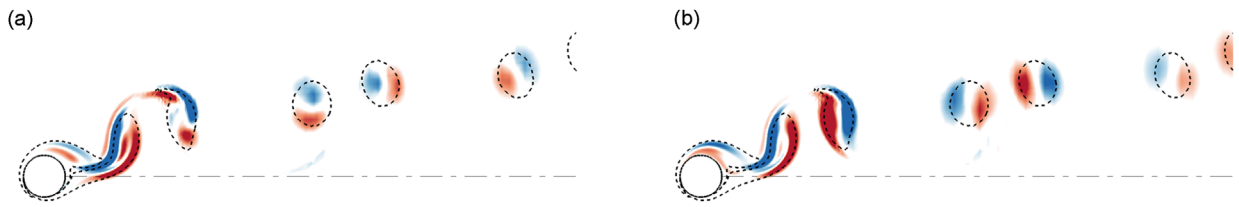

Fig. 11. Spanwise perturbation vorticity contours at $\alpha=1.85$, $\mathrm{Re}=300$ for the spanwise wavelengths specified. Contour shading as per Fig. 3. Flow is from left to right and the cylinder is rotating anticlockwise. (a) Mode G at $\lambda/D=20$, $\mu=1.002$. (b) Mode A at $\lambda/D=3.75$, $\mu=1.052$.

Table 1
Summary of the modes showing the characteristic wavelength, nature of the Floquet multiplier (μ), the periodicity of the two-dimensional base flow and the spatial symmetries of these modes with respect to the streamwise velocity, u.

Mode	λ/D	Nature of μ	Base flow	Symmetry
A	$\simeq 4$	Real and positive	Mode I shedding	$u(x,y,z,t)=u(x,y,z+n\lambda,t+T)$
B	$\simeq 0.8$	Real and positive	Mode I shedding	$u(x,y,z,t)=u(x,y,z+n\lambda,t+T)$
C	$\simeq 1$	Real and negative	Mode I shedding	$u(x,y,z,t)=u(x,y,z+n\lambda,t+2T)$
D	$\simeq 1.9$	Real and positive	Mode I shedding	$u(x,y,z,t)=u(x,y,z+n\lambda,t+T)$
E	$[1.4-12]$	Real and positive	Steady state I	$u(x,y,z,t)=u(x,y,z+n\lambda)$
E′	$[2.4-3.6]$	Real and positive	Steady state II	$u(x,y,z,t)=u(x,y,z+n\lambda)$
F	$\simeq 0.4$	Complex	Steady state I	$u(x,y,z,t)=u(x,y,z+n\lambda,t+T_{3D})$
F′	$\simeq 0.3$	Complex	Steady state II	$u(x,y,z,t)=u(x,y,z+n\lambda,t+T_{3D})$
G	$\simeq 18$	Real and positive	Mode I shedding	$u(x,y,z,t)=u(x,y,z+n\lambda,t+T)$

3.10. Mode G instability

Returning to the BvK vortex street, at rotation rates of $\alpha\simeq 1.85$, a long wavelength instability is observed for $\mathrm{Re}\gtrsim 280$. This mode has spatio-temporal characteristics similar to the mode A instability. In Fig. 11 are the perturbation vorticity contours of mode G and mode A at $\alpha=1.85$, $\mathrm{Re}=340$ showing this comparison. Mode G occurs alongside modes A and C, with a very low growth rate as seen in Fig 23 of Rao et al. (2013a).

4. Conclusions

Numerical and experimental investigations have been performed to characterise and quantify the wake of a rotating cylinder for rotation rates $\alpha\leq 7$ and Reynolds numbers $\mathrm{Re}\leq 400$. Using linear stability analysis, the various two- and three-dimensional transitions that occur within this parameter space have been identified. Two unsteady regimes exist: (a) mode I shedding for $\alpha\lesssim 2$ which is characterised by alternate vortex shedding and (b) mode II shedding occurring over a small range of α at higher rotation rates and characterised by single sided vortex shedding (Stojković et al., 2002, 2003; Mittal and Kumar, 2003 and others). Two steady states have also been identified: steady state I and steady state II (Mittal and Kumar, 2003; Pralits et al., 2010; Rao et al., 2013b). Steady state I occurs at lower Reynolds numbers and steady state II occurs at higher rotation rates beyond the mode II shedding region. These two steady states can be distinguished by the flow features such as the location in the stagnation point and the drag coefficient.

For low rotation rates ($\alpha\lesssim 1$), the transitions are similar to the non-rotating case. On increasing the Reynolds number, the flow first becomes unsteady following which the transition to three-dimensionality occurs via the mode A instability followed by the transition to mode B at higher Reynolds numbers. However, the onset of these modes is delayed to higher values of Reynolds numbers as the rotation rate is increased from $\alpha=0$ to $\alpha=1$.

At slightly higher rotation rates ($1.5\lesssim\alpha\lesssim 1.9$), the onset of unsteady flow is delayed to higher Reynolds numbers, and the wake becomes increasingly asymmetric as the rotation rate is increased. Previous studies (Blackburn and Sheard, 2010) have shown that the asymmetry of the wake can give rise to subharmonic modes. Here, mode C, a subharmonic mode, is observed for $\alpha\geq 1.5$ and $\mathrm{Re}\gtrsim 250$. Two other modes, mode D and mode G, are observed for $\alpha\gtrsim 1.85$. These modes have similar spatio-temporal characteristics of the mode A instability, but vastly different spanwise wavelengths. Mode D has an average spanwise wavelength of approximately $2D$, while mode G has a much longer average spanwise wavelength of $\simeq 18D$.

For $\alpha\gtrsim 2$, vortex shedding is suppressed until higher rotation rates, where mode II shedding is observed. On this steady state (SSI), two three-dimensional modes are observed: mode E and mode F. Mode E is believed to arise out of a hyperbolic instability, while the physical mechanism of mode F is attributed to a centrifugal instability of the shear layers. Mode F introduces a spanwise frequency in the wake and recent experimental analysis (Radi et al., 2013) shows that mode F is a travelling wave with a frequency that is accurately predicted by the linear stability analysis.

Previously unpublished results show that mode E is observed at lower rotation rates ($\alpha \lesssim 1.9$), when the two-dimensional base flow is artificially stabilised. Under these conditions, mode E was observed at $\mathrm{Re} \simeq 100$ for the non-rotating cylinder. The spatio-temporal characteristics of mode E bear close resemblance to the three-dimensional mode observed in the steady wake behind cylinders translating along a wall.

At higher rotation rates beyond the mode II shedding regime, modes E′ and F′, are observed on steady state II base flow. These modes have spatio-temporal characteristics similar to their counterparts on steady state I base flow.

The characteristics of the modes observed in the parameter space are summarised in Table 1. The average spanwise wavelength, nature of the Floquet multiplier, the two-dimensional base flow on which these modes occur and the spatio-temporal symmetry are detailed here.

Some of the three-dimensional modes which are predicted by linear stability analysis have been observed experimentally. The saturated state of the experimentally observed wake was found to be in good agreement with the linear predictions.

Acknowledgements

The support from Australian Research Council Discovery Grant nos. DP0877327, DP110102141, DP110100434 and DP130100822 and computing time from the National Computational Infrastructure (NCI), the Victorian Life Sciences Computation Initiative (VLSCI), iVEC@Murdoch and the Monash Campus Cluster are gratefully acknowledged.

References

Akoury, R.E., Braza, M., Perrin, R., Harran, G., Hoarau, Y., 2008. The three-dimensional transition in the flow around a rotating cylinder. Journal of Fluid Mechanics 607, 1–11.

Balcarová, L., 2011. Experimental investigation of shedding mode II in circular cylinder wake. In: Czech Technical University Student's Conference, Prague, pp. 1–16.

Barkley, D., Henderson, R.D., 1996. Three-dimensional Floquet stability analysis of the wake of a circular cylinder. Journal of Fluid Mechanics 322, 215–241.

Blackburn, H.M., Lopez, J.M., 2003. On three-dimensional quasiperiodic Floquet instabilities of two-dimensional bluff body wakes. Physics of Fluids 15, L57–L60.

Blackburn, H.M., Marques, F., Lopez, J.M., 2005. Symmetry breaking of two-dimensional time-periodic wakes. Journal of Fluid Mechanics 552, 395–411.

Blackburn, H.M., Sheard, G.J., 2010. On quasiperiodic and subharmonic Floquet wake instabilities. Physics of Fluids 22. 031701-1–031701-4.

Hourigan, K., Rao, A., Brøns, M., Leweke, T., Thompson, M.C., 2013. Vorticity generation and wake transition for a translating circular cylinder: wall proximity and rotation effects. Journal of Wind Engineering and Industrial Aerodynamics 122, 2–9.

Kang, S.M., Choi, H.C., Lee, S., 1999. Laminar flow past a rotating circular cylinder. Physics of Fluids 11, 3312–3321.

Karniadakis, G.E., Sherwin, S.J., 2005. Spectral/hp Methods for Computational Fluid Dynamics. Oxford University Press, Oxford.

Kumar, S., Cantu, C., Gonzalez, B., 2011. Flow past a rotating cylinder at low and high rotation rates. Journal of Fluids Engineering 133, 041201.

Leontini, J.S., Jacono, D.L., Thompson, M.C., 2013. Wake states and frequency selection of a streamwise oscillating cylinder. Journal of Fluid Mechanics 730, 162–192.

Leontini, J.S., Thompson, M.C., Hourigan, K., 2007. Three-dimensional transition in the wake of a transversely oscillating cylinder. Journal of Fluid Mechanics 577, 79–104.

Leweke, T., Williamson, C.H.K., 1998. Cooperative elliptic instability of a vortex pair. Journal of Fluid Mechanics 360, 85–119.

Lo Jacono, D., Leontini, J., Thompson, M.C., Sheridan, J., 2010. Modification of three-dimensional transition in the wake of a rotationally oscillating cylinder. Journal of Fluid Mechanics 643, 349–362.

Meena, J., Sidharth, G.S., Khan, M.H., Mittal, S., 2011. Three dimensional instabilities in flow past a spinning and translating cylinder. In: IUTAM Symposium on Bluff Body Flows, pp. 59–62.

Mittal, S., 2001. Flow past rotating cylinders: effect of eccentricity. Journal of Applied Mechanics 68, 543–552.

Mittal, S., 2004. Three-dimensional instabilities in flow past a rotating cylinder. Journal of Applied Mechanics 71, 89–95.

Mittal, S., Kumar, B., 2003. Flow past a rotating cylinder. Journal of Fluid Mechanics 476, 303–334.

Pralits, J.O., Brandt, L., Giannetti, F., 2010. Instability and sensitivity of the flow around a rotating circular cylinder. Journal of Fluid Mechanics 650, 513–536.

Pralits, J.O., Giannetti, F., Brandt, L., 2013. Three-dimensional instability of the flow around a rotating circular cylinder. Journal of Fluid Mechanics 730, 5–18.

Prandtl, L., 1926. Application of the “Magnus Effect” to the Wind Propulsion of Ships. Technical memorandum, National Advisory Committee for Aeronautics.

Radi, A., Thompson, M.C., Rao, A., Hourigan, K., Sheridan, J., 2013. Experimental evidence of new three-dimensional modes in the wake of a rotating cylinder. Journal of Fluid Mechanics 734, 567–594.

Rao, A., Leontini, J., Thompson, M.C., Hourigan, K., 2013a. Three-dimensionality in the wake of a rotating cylinder in a uniform flow. Journal of Fluid Mechanics 717, 1–29.

Rao, A., Leontini, J.S., Thompson, M.C., Hourigan, K., 2013b. Three-dimensionality in the wake of a rapidly rotating cylinder in uniform flow. Journal of Fluid Mechanics 730, 379–391.

Rao, A., Stewart, B., Thompson, M.C., Leweke, T., Hourigan, K., 2011. Flows past rotating cylinders next to a wall. Journal of Fluids and Structures 27, 668–679.

Rao, A., Thompson, M.C., Leweke, T., Hourigan, K., 2013c. The flow past a circular cylinder translating at different heights above a wall. Journal of Fluids and Structures 41, 9–21.

Rao, A., Thompson, M.C., Leweke, T., Hourigan, K., 2013d. Dynamics and stability of the wake behind tandem cylinders sliding along a wall. Journal of Fluid Mechanics 722, 291–316.

Robichaux, J., Balachandar, S., Vanka, S.P., 1999. Three-dimensional Floquet instability of the wake of a square cylinder. Physics of Fluids 11, 560–578.

Ryan, K., Thompson, M.C., Hourigan, K., 2005. Three-dimensional transition in the wake of bluff elongated cylinders. Journal of Fluid Mechanics 538, 1–29.

Sheard, G.J., 2011. Wake stability features behind a square cylinder: focus on small incidence angles. Journal of Fluids and Structures 27, 734–742.

Sheard, G.J., Fitzgerald, M.J., Ryan, K., 2009. Cylinders with square cross-section: wake instabilities with incidence angle variation. Journal of Fluid Mechanics 630, 43–69.

Sheard, G.J., Thompson, M.C., Hourigan, K., 2003. From spheres to circular cylinders: the stability and flow structures of bluff ring wakes. Journal of Fluid Mechanics 492, 147–180.

Sheard, G.J., Thompson, M.C., Hourigan, K., 2004a. Asymmetric structure and non-linear transition behaviour of the wakes of toroidal bodies. European Journal of Mechanics—B/Fluids 23, 167–179.

Sheard, G.J., Thompson, M.C., Hourigan, K., 2004b. From spheres to circular cylinders: non-axisymmetric transitions in the flow past rings. Journal of Fluid Mechanics 506, 45–78.
Sheard, G.J., Thompson, M.C., Hourigan, K., 2005. Subharmonic mechanism of the mode C instability. Physics of Fluids 17, 1–4.
Stewart, B.E., Hourigan, K., Thompson, M.C., Leweke, T., 2006. Flow dynamics and forces associated with a cylinder rolling along a wall. Physics of Fluids 18. 111701-1–111701-4.
Stewart, B.E., Thompson, M.C., Leweke, T., Hourigan, K., 2010. The wake behind a cylinder rolling on a wall at varying rotation rates. Journal of Fluid Mechanics 648, 225–256.
Stojković, D., Breuer, M., Durst, F., 2002. Effect of high rotation rates on the laminar flow around a circular cylinder. Physics of Fluids 14, 3160–3178.
Stojković, D., Schon, P., Breuer, M., Durst, F., 2003. On the new vortex shedding mode past a rotating circular cylinder. Physics of Fluids 15, 1257–1260.
Thompson, M.C., Hourigan, K., Cheung, A., Leweke, T., 2006. Hydrodynamics of a particle impact on a wall. Applied Mathematical Modelling 30, 1356–1369.
Thompson, M.C., Hourigan, K., Sheridan, J., 1996. Three-dimensional instabilities in the wake of a circular cylinder. Experimental Thermal and Fluid Science 12, 190–196.
Thompson, M.C., Leweke, T., Williamson, C.H.K., 2001. The physical mechanism of transition in bluff body wakes. Journal of Fluids and Structures 15, 607–616.
Williamson, C.H.K., 1988. The existence of two stages in the transition to three-dimensionality of a cylinder wake. Physics of Fluids 31, 3165–3168.
Williamson, C.H.K., 1996a. Three-dimensional wake transition. Journal of Fluid Mechanics 328, 345–407.
Williamson, C.H.K., 1996b. Vortex dynamics in the cylinder wake. Annual Review of Fluid Mechanics 28, 477–539.
Wu, J., Sheridan, J., Hourigan, K., Soria, J., 1996a. Shear layer vortices and longitudinal vortices in the near wake of a circular cylinder. Experimental Thermal and Fluid Science 12, 169–174.
Wu, J., Sheridan, J., Welsh, M.C., Hourigan, K., 1996b. Three-dimensional vortex structures in a cylinder wake. Journal of Fluid Mechanics 312, 201–222.
Wu, J., Sheridan, J., Welsh, M.C., Hourigan, K., Thompson, M.C., 1994. Longitudinal vortex structures in a cylinder wake. Physics of Fluids 6, 2883–2885.
Yildirim, I., Rindt, C.C.M., van Steenhoven, A.A., 2013a. Energy contents and vortex dynamics in Mode-C transition of wired-cylinder wake. Physics of Fluids 25, 054103-1–054103-18.
Yildirim, I., Rindt, C.C.M., van Steenhoven, A.A., 2013b. Mode C flow transition behind a circular cylinder with a near-wake wire disturbance. Journal of Fluid Mechanics 727, 30–55.
Zhang, H., Fey, U., Noack, B.R., Konig, M., Eckelemann, H., 1995. On the transition of the cylinder wake. Physics of Fluids 7, 779–794.